

# 3D Porous Carbon Sheets with Multidirectional Ion Pathways for Fast and Durable Lithium–Sulfur Batteries

Gaoran Li, Wen Lei, Dan Luo, Ya-Ping Deng, Deli Wang,\* and Zhongwei Chen\*

In this work, unique porous carbon sheets (PCSs) are developed via a facile synthesis. The obtained PCS delivers long-range conductive framework, abundant active interfaces, rich element doping, and notably a high inner porosity that builds up an admirable 3D network for multidirectional ion transfer. Such unique architecture and surface chemistry enable ultrafast sulfur electrochemistry as well as high-efficiency inhibition on polysulfide shuttling via the dually physical and chemical sulfur confinement. The PCS-based sulfur electrodes achieve superb rate capability up to 10 C, outstanding cyclability over 1000 cycles, and high areal capacity of 4.8 mA h cm<sup>-2</sup>. This work offers an appealing model of material engineering for fast and reliable lithium–sulfur batteries, as well as guidance for rational structural design in extended energy storage and conversion systems.

## 1. Introduction

Lithium–sulfur (Li–S) batteries are drawing increasingly extensive research enthusiasms in pursuit of next-generation energy storage, as the currently dominant lithium-ion batteries based on intercalation electrochemistry are approaching their theoretical capacity limits.<sup>[1]</sup> Li–S electrochemistry realized by coupling elemental sulfur and metallic lithium enables an attractively high-energy density of 2600 W h kg<sup>-1</sup>, which quintuples that of the conventional LIB.<sup>[2]</sup> Moreover, the abundance of natural resources, intrinsic environmental benignity, and facile fabrication endows Li–S batteries with great promise in high-energy applications such as smart grid and electric vehicles.<sup>[3]</sup> However,

several stubborn obstructions including the insulating nature of elemental sulfur and lithium sulfide, the large volume variation during cycling, and the shuttling behaviors of intermediate polysulfides, are still haunting Li–S batteries with poor sulfur utilization, low practical energy density, and unsatisfactory lifespan, which are seriously hindering the pace of Li–S commercialization.<sup>[4]</sup>

The past few decades have witnessed enormous research efforts that were devoted to overcome these problems, among which the rational design of sulfur electrode is of particular significance in boosting Li–S performance.<sup>[5]</sup>

Sulfur host is required to offer favorable

electronic/ionic conductivity, strong sulfur confinement, and robust mechanical integrity to ensure reversible sulfur electrochemistry. Graphene, as a representative 2D carbon material, has triggered a research fever since its birth in 2004 due to its unique physical, electrical, thermal, and mechanical properties.<sup>[6]</sup> As sulfur host, graphene-based architecture delivers considerable superiorities of high conductivity, light weight, and excellent mechanical robustness, which has been widely explored for enhanced Li–S performance.<sup>[7]</sup> However, the intact and planar carbon lattice of graphene determines its lack of porosity, which is capable of providing neither strong sulfur confinement, nor sufficient surface area for sulfur or lithium sulfide deposition during the cycling. Apart from that, in spite of its excellent conductivity in the extending direction of carbon lattice, such nonporous 2D structure results in poor vertical ion transfer due to the lack of vertical pathway for ion diffusion, which severely restrains the sulfur redox kinetics.<sup>[8]</sup> Under such circumstances, porous 2D carbon materials, which deliver remarkable structural plasticity, serve as appealing candidates to afford high porosity and abundant vertical ion pathways while retaining the favorable characteristics such as long-range conductivity and good mechanical performance.<sup>[9]</sup> Whereas the current synthesis of porous 2D carbon materials generally involves complicated procedures and harsh conditions such as postactivation process and the use of hazardous acids for the template removal, which is awfully challenging for practical application.<sup>[10]</sup>

Herein, we developed a unique porous carbon sheets (PCSs) through a facial synthesis by simply using P<sub>2</sub>O<sub>5</sub> as the self-sacrificing template. The obtained PCS exhibits elegant large-area 2D morphology with high meso/microporosity and rich element doping of phosphorous and oxygen. When employed

Dr. G. Li, D. Luo, Y.-P. Deng, Prof. Z. Chen  
Department of Chemical Engineering  
Waterloo Institute for Nanotechnology  
Waterloo Institute for Sustainable Energy  
University of Waterloo  
Waterloo, Ontario N2L 3G1, Canada  
E-mail: zhwchen@uwaterloo.ca

W. Lei, Prof. D. Wang  
Key laboratory of Material Chemistry for Energy Conversion and Storage  
(Huazhong University of Science and Technology)  
Ministry of Education  
Hubei Key Laboratory of Material Chemistry and Service Failure  
School of Chemistry and Chemical Engineering  
Huazhong University of Science and Technology  
Wuhan 430074, P. R. China  
E-mail: wangdl81125@hust.edu.cn

 The ORCID identification number(s) for the author(s) of this article can be found under <https://doi.org/10.1002/aenm.201702381>.

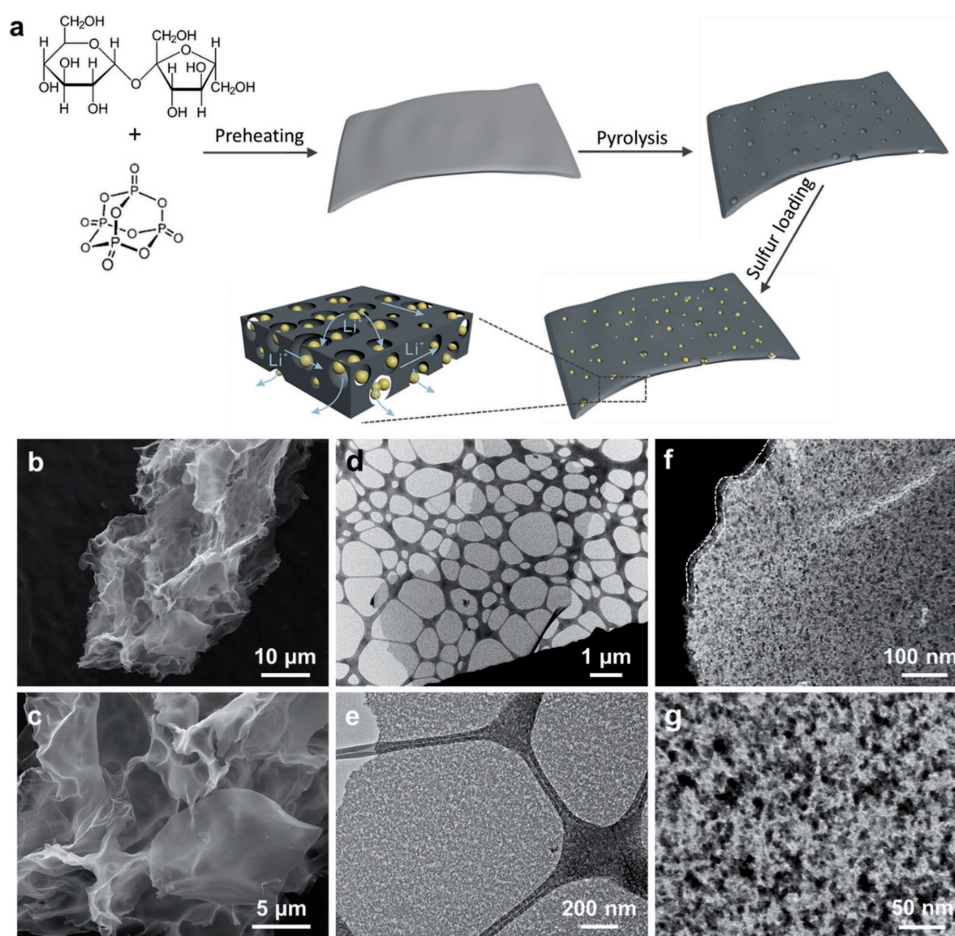
DOI: 10.1002/aenm.201702381

as sulfur host, the large-area and highly porous texture enables excellent long-range conductivity, abundant active interfaces, and strong physical sulfur confinement. More importantly, the highly porous structure introduces an interconnected 3D framework for ion transfer through the carbon matrix, overcoming the sluggish vertical ionic conductivity in graphene and realizing expedite ion transfer within the electrode for fast and efficient sulfur electrochemistry. Beyond that, the abundant P and O doping in carbon lattice contributes to a significantly polarized surface, which offers further sulfur immobilization via the favorable chemical interactions with sulfur species. Attributed to these featuring superiorities, the PCS-based sulfur electrodes achieve outstanding cyclability with a negligible capacity fading rate of 0.025% per cycle over 1000 cycles, superb rate capability up to 10 C, high sulfur content up to 90 wt%, and reversible areal capacity of 4.8 mA h cm<sup>-2</sup> under high sulfur loading of 5.5 mg cm<sup>-2</sup>.

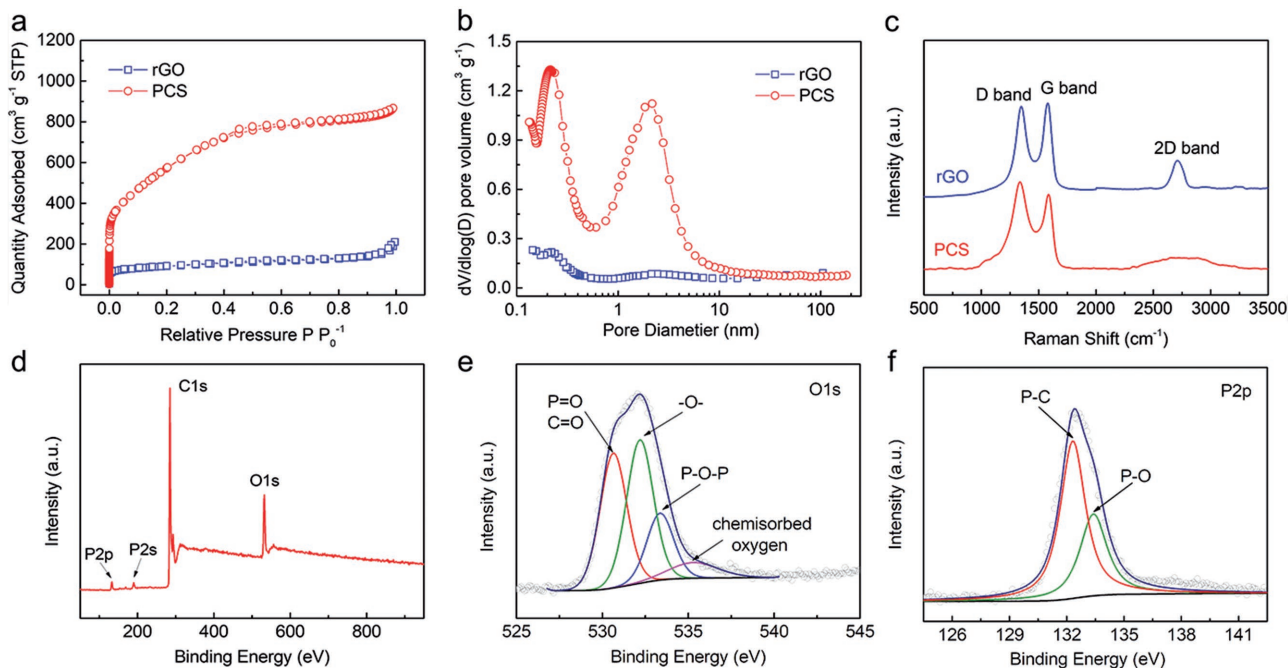
## 2. Results and Discussion

Figure 1a briefly illustrates the synthetic process of PCS and according to sulfur composite. First, the mixture of sucrose and P<sub>2</sub>O<sub>5</sub> in weight ratio of 2:6 was prethermally treated at 200 °C for 6 h in a sealed reactor. The obtained product achieves a

sheet-like morphology attributed to the templating effect by the polymerized phosphoric acid that formed during the thermal process (Figure S1, Supporting Information). This precursor was subsequently pyrolyzed at 450 °C and 900 °C for 1 and 3 h respectively under Ar atmosphere to yield the final product. Figure 1b,c shows the evidential 2D morphology of the as-developed PCS, which is similar to that of reduced graphene oxide (rGO, Figure S2a, Supporting Information) obtained through thermal reduction under the same condition. The large-area PCS intertwines into an interconnected porous framework. The 2D structure was further confirmed by transmission electron microscope (TEM) observation as shown in Figure 1d. The size of PCS can reach tens of micrometers in diameter, while its thickness is around 20–30 nm as verified by atomic force microscope (AFM) analysis (Figure S3, Supporting Information). Notably, in stark contrast to the intact and smooth morphology of rGO sheets (Figure S2b, Supporting Information), the obtained PCS shows numerous disordered pores scattering inside the sheets as shown in Figure 1e. High-resolution TEM and selected area diffraction images were shown in Figure S4 (Supporting Information), where no obvious crystal fringe or diffraction rings were observed, indicating the amorphous structure of the obtained PCS. The dark field TEM characterization gives a clearer observation of the highly porous architecture of the PCS (Figure 1f,g). The thickness of the PCS is observed



**Figure 1.** a) Schematic diagram of the preparation of PCS and S@PCS composite, the SEM b,c), TEM d,e), and dark field TEM f,g) observations of PCS.



**Figure 2.** The isotherms a), pore distributions b), and Raman spectra c) of PCS and rGO. The XPS survey d), O1s e), and P2p spectra f) of PCS.

around 20 nm, which is consistent with the AFM result. The massive porous structures interpenetrate and interconnect with each other, thus building up a 3D architecture for ion transfer inside and through the PCS, which potentially offers a significant improvement of ion supply for energy storage applications. Besides, the large-area carbon sheets also intertwine together building up an interconnected conductive framework to offer fast electron transfer. The bulk electrical conductivity of the obtained PCS was measured around  $20 \text{ S cm}^{-1}$ , which is among the top level of amorphous carbon materials.<sup>[11]</sup> Based on this result,  $\text{N}_2$  adsorption/desorption measurement was performed to investigate the structural difference between rGO and the as-developed PCS. As shown in **Figure 2a**, the isotherm of PCS exhibits a significant adsorption/desorption behavior at medium and low range of relative pressure, indicating its abundance in mesopores and micropores. The hierarchical porosity of PCS is also supported by the evident peaks at 0.22 and 2.2 nm in the pore size distribution (**Figure 2b**). Comparatively, the much weaker behaviors in both isotherm and pore size distribution of rGO manifest its conspicuously less porosity than PCS, which is consistent with the TEM comparison. The as-developed PCS delivers a specific surface area of  $2027.7 \text{ m}^2 \text{ g}^{-1}$  and pore volume of  $1.33 \text{ cm}^3 \text{ g}^{-1}$ , which are overwhelmingly higher than those of rGO ( $332.0 \text{ m}^2 \text{ g}^{-1}$  and  $0.32 \text{ cm}^3 \text{ g}^{-1}$ , respectively). These results give a convincing proof of the successful pore construction in the 2D carbon sheets to overcome the lack of porosity in graphene. The porosity of PCS is proposed originating from two aspects: (i) during the first pyrolysis stage at  $450 \text{ }^\circ\text{C}$ , the phosphoric acid that formed through the dehydration reactions constantly etches the carbon skeleton to form microporous structure; (ii) during the high-temperature pyrolysis at  $900 \text{ }^\circ\text{C}$ , the residual  $\text{P}_2\text{O}_5$  and phosphoric acid were reduced by carbon to form red phosphorous, which

subsequently sublimates and leaves abundant mesopores in the final product. As a result, the step-wise multistage templating contributes to the elegant 2D morphology and well-defined hierarchically porous texture of PCS.

Raman analysis was performed to study the microstructure of PCS. As shown in **Figure 2c**, both rGO and PCS show two sharp peaks at  $1348 \text{ cm}^{-1}$  and  $1580 \text{ cm}^{-1}$ , which refer to the breathing vibration of the hybridized carbon rings and the stretching vibration of  $\text{sp}^2$  carbon atom pairs, respectively.<sup>[12]</sup> The higher intensity ratio of D band to G band ( $I_D/I_G$ ) indicates more defects in PCS compared to that in rGO, which implies its abundant element doping.<sup>[13]</sup> Moreover, comparing to the sharp 2D peak of rGO, the bump at around  $2700 \text{ cm}^{-1}$  in PCS Raman spectrum indicates its higher sheet thickness, which is consistent with the previous AFM and TEM results.<sup>[14]</sup> The element doping of PCS was verified by element mapping, which shows a uniformly dispersed P and O in the carbon matrix (**Figure S5**, Supporting Information). X-ray photoelectron spectroscopy (XPS) analysis was performed to study the surface chemistry of PCS. The element survey confirms the existences of P and O in PCS as shown in **Figure 2d**. The high-resolution O1s spectrum (**Figure 2e**) shows overlapped peaks, which can be fitted into four peaks ascribing to the  $\text{P=O/C=O}$  ( $530.6 \text{ eV}$ ),  $-\text{O}-$  ( $532.2 \text{ eV}$ ), and  $\text{P-O-P}$  ( $533.4 \text{ eV}$ ) bonding, as well as the chemisorbed oxygen ( $535.4 \text{ eV}$ ).<sup>[15]</sup> Meanwhile, the fitting of P2p spectrum (**Figure 2f**) is resolved into two peaks locating at  $132.3$  and  $133.5 \text{ eV}$ , which were assigned to the  $\text{P-C}$  and  $\text{P-O}$  bonding respectively. These results strongly manifest that the phosphorus and oxygen are successfully doped into the carbon lattice. The P and O content in PCS is 3.5% and 11.7% respectively according to the XPS results.

The above results have revealed the well-developed porosity and rich element doping in PCS. Such structural

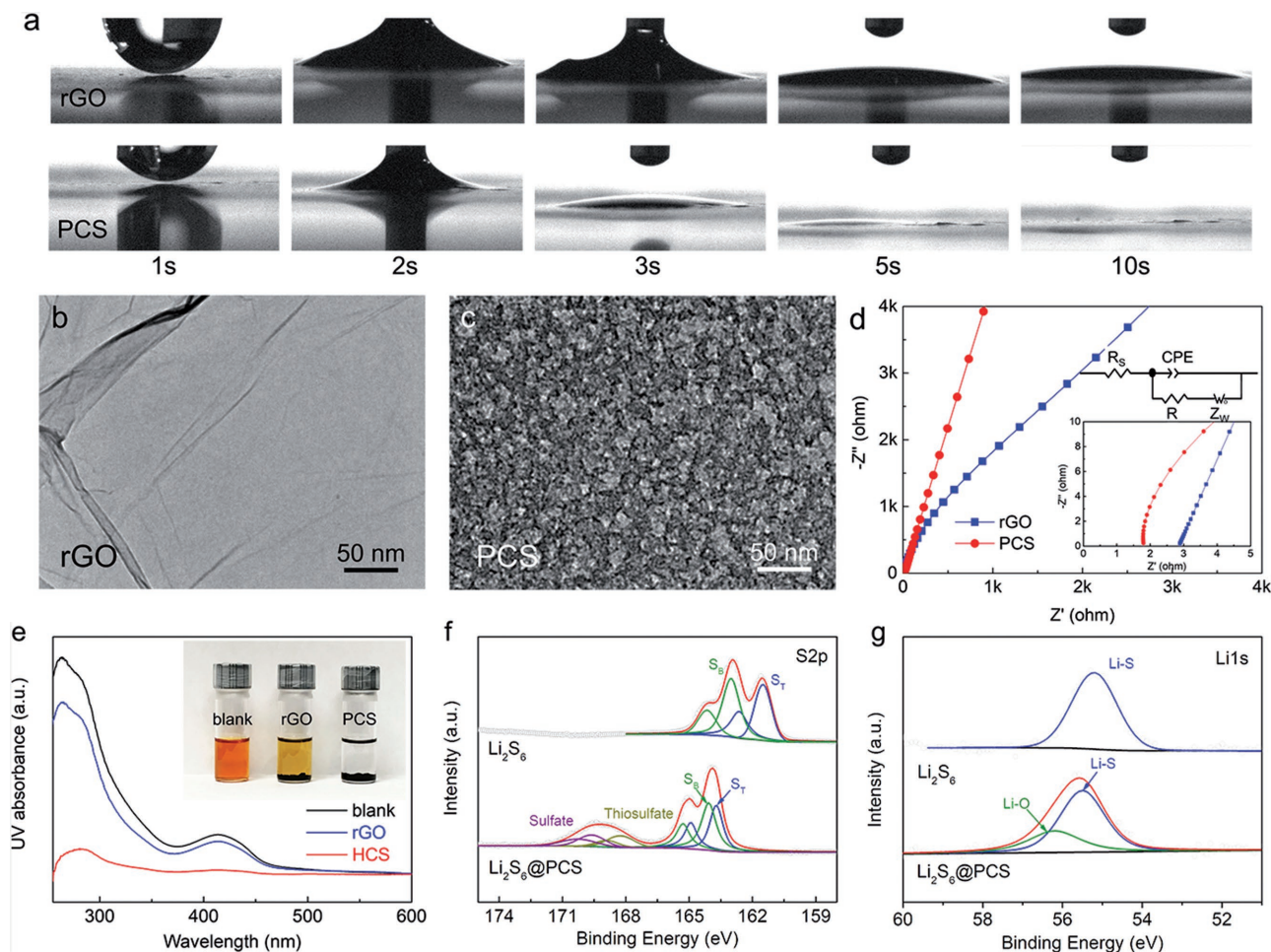


**Figure 3.** a) The electrolyte infiltration comparison between rGO and PCS; the high-resolution surface TEM observations of PCS b) and rGO c), the EIS analysis of electrolyte-infiltrated rGO and PCS layer, e) the UV-vis spectra and optical images of polysulfide solutions adsorbed by rGO and PCS, the S2p f) and Li1s g) spectra of polysulfide before and after adsorption.

superiorities are considered beneficial to the ion transfer within the carbon matrix and thus can improve the sulfur electrochemical redox in Li-S batteries. Electrolyte infiltration evaluations were performed to investigate the electrolyte wettability to rGO and PCS. As shown in **Figure 3a**, the electrolyte (1 M lithium bis(trifluoromethanesulfonyl) imide (LiTFSI) in binary solvent of 1,2-dimethoxyethane (DEM) and 1,3-dioxolane (DOL) with 0.2 M  $\text{LiNO}_3$  as additive) drop can still be clearly observed on the rGO surface even after 10 s, while PCS accomplishes an almost complete electrolyte infiltration within 5 s. This result strongly illustrates the much faster electrolyte infiltration in PCS, which is attributed to its higher surface polarity benefiting from the abundant P and O doping. The high-resolution TEM observation clearly reveals the massive porous structures in PCS (**Figure 3b**), which interpenetrate with each other to offer interconnected pathways allowing fluent ion transfer within as well as through the PCS matrix. By contrast, rGO delivers a flat and smooth surface where ions can only perform planar diffusion but hardly in vertical direction (**Figure 3c**). The overall  $\text{Li}^+$  transfer performances in PCS and rGO matrix were studied by electrochemical impedance spectroscopy (EIS) analysis as shown in **Figure 3d**. When soaking the carbon layer with

Li-S electrolyte, the smaller intercept in real-part axis for PCS indicates its smaller solution resistant corresponding to the improved electrolyte wettability, which is consistent to the electrolyte-infiltration result. Meanwhile, the much higher slope in low-frequency range manifests the much faster  $\text{Li}^+$  diffusion in PCS, which benefits from the multidirectional ion pathways built by the massive porous structures. All these results evidentially support the significantly improved  $\text{Li}^+$  transfer in PCS, which is promising to enable a fast sulfur electrochemistry in Li-S batteries.

Apart from that, such highly porous and P-, O-rich construction also serves as a potentially strong sulfur immobilizer to inhibit the polysulfide shuttling in Li-S batteries. As a proof of concept, rGO and PCS were immersed into polysulfide solution (the blank sample in **Figure 3e**,  $5 \times 10^{-3}$  M  $\text{Li}_2\text{S}_6$  in electrolyte) to investigate their adsorptions to sulfur species. After immersion for 12 h, the polysulfide solution with PCS shows a much lighter and transparent color than that with rGO (**Figure 3e**). Meanwhile, the UV-vis test also reveals the much lower polysulfide residuals in PCS-based solution by showing much weaker peaks at around 280 and 415 nm, which are assigned to  $\text{S}_6^{2-}$  and  $\text{S}_4^{2-}$  respectively.<sup>[16]</sup> These results visually and directly

demonstrate that the as-developed PCS holds a much higher capability of polysulfide adsorption than rGO. The superior polysulfide adsorption of PCS is attributed to its combined physical and chemical sulfur confinements. The highly porous PCS matrix offers strong spatial restriction to confine the sulfur species inside the pores, while the P and O doping enhances the surface polarity so that the polysulfides can be chemically anchored on the PCS surface to further boosts the absorbability. Besides, the high surface area offers abundant active sites for these physical and chemical interactions between PCS and sulfur species. The chemical polysulfide adsorption was further studied by XPS analysis as shown in Figure 3f,g. The S2p spectrum of pristine  $\text{Li}_2\text{S}_6$  shows typically two pairs of peaks locating at 161.5 and 163.0 eV, referring to the terminal ( $\text{S}_\text{T}$ ) and bridging sulfur ( $\text{S}_\text{B}$ ) respectively.<sup>[17]</sup> After adsorption, the S2p spectrum of the sulfur species in PCS (denoted as  $\text{Li}_2\text{S}_6$ @PCS) exhibits similarly two pairs of peaks but with a considerable shifting to higher binding energy range, which illustrates the reduction of electron cloud density in the sulfur atoms as a result of the formation of the lithium bond bridging sulfur and doping elements.<sup>[2b,18]</sup> Meanwhile, a pair of overlapped peaks emerges at higher binding energy around 169.5 eV, which is ascribed to the sulfur–oxygen bonding in sulfate and thiosulfate.<sup>[19]</sup> The Li1s spectrum of polysulfide also undergoes a shift to higher binding energy after adsorption, while a new peak referring to lithium–oxygen (Li–O) bonding appears. Moreover, the P2p spectra of PCS witnessed a considerable signal enhancement of P–O bonding after polysulfide adsorption (Figure S6, Supporting Information), which may be attributed to the overlying of P–S signal considering that the binding energy of P–O and P–S are close.<sup>[20]</sup> Meanwhile, a slight peak shift to lower binding energy can be observed for the P–O peak, which support the possible P–S bonding between PCS and polysulfide.<sup>[21]</sup> These variations in XPS spectra serve as strong evidences of the chemical interactions between PCS and sulfur species. On the basis of the above results, PCS combines strong physical and chemical confinement to sulfur species and is highly promising as sulfur immobilizer to inhibit polysulfide shuttling and improve Li–S battery performance.

Electrochemical evaluations were conducted to verify the advantageous effects of PCS on Li–S batteries. The sulfur–carbon composite (denoted as S@PCS) was prepared through the conventional melt-impregnation method. The sulfur content in composite is 70 wt%. The sulfur electrode was fabricated through the slurry-casting process (see details in the Supporting Information). Sulfur electrode based on rGO (S@rGO) was prepared via the same process for comparison. After sulfur loading, sharp peaks referring to element sulfur emerge in the X-ray diffraction (XRD) pattern of S@PCS in contrast to the amorphous PCS (Figure S7a, Supporting Information). Meanwhile, the isotherms also witness a drastic porosity decline from PCS to S@PCS (Figure S7b, Supporting Information). The uniform sulfur distribution in S@PCS is verified by TEM observation and element mapping as shown in Figure S8 (Supporting Information). All these results strongly manifest that sulfur successfully and uniformly infiltrates and occupies the pores in the PCS matrix.

Galvanostatic charge–discharge shows typical two-plateau voltage profiles for both S@PCS and S@rGO electrodes

(Figure 4a). The high-potential discharge plateau at around 2.35 V (vs  $\text{Li}^+/\text{Li}$ , hereafter inclusive) is attributed to the electroreduction of elemental sulfur into soluble long-chain polysulfide ( $\text{Li}_2\text{S}_x$ ,  $6 \leq x \leq 8$ ), while the long discharge plateau at  $\approx 2.1$  V corresponds to the further reduction of the polysulfide anions to form insoluble  $\text{Li}_2\text{S}_2$  and  $\text{Li}_2\text{S}$ . The electrode charging performs an inverse process. The cyclic voltammetry (CV) curves are consistent with the voltage profiles by showing two cathodic peaks and overlapped anodic peaks (Figure 4b). It is worth noting that S@PCS electrode delivers much smaller potential hysteresis in both voltage profile and CV curve compared to those of S@rGO electrode, implying its smaller electrochemical polarization and faster reaction kinetics. Galvanostatic cycling at C/5 rate ( $1\text{C} = 1675 \text{ mA g}^{-1}$ ) were performed to investigate their cyclabilities. S@PCS electrode delivers a high initial capacity of  $1344 \text{ mA h g}^{-1}$ , which is over 80% of its theoretical maximum, and retains  $1017 \text{ mA h g}^{-1}$  after 50 cycles. By contrast, S@rGO electrode shows a much lower initial capacity of  $1136 \text{ mA h g}^{-1}$  and undergoes a fast capacity fading to  $657.6 \text{ mA h g}^{-1}$  after 50 cycles (Figure 4c). The superior cycling performance of S@PCS electrode is attributed to its high-efficiency shutting inhibition benefited from the combined physical and chemical sulfur immobilization as verified above. Self-discharge behavior is an important indicator of the polysulfide shuttling level in Li–S batteries. As shown in Figure 5a, sulfur electrodes were rested for 24 h after the first cycle to study their self-discharge rates. In comparison to S@rGO, S@PCS electrode exhibits a much steadier voltage retention during the battery rest (Figure 5b) and significantly less capacity loss as demonstrated by the subsequent discharge after rest (Figure 5c), which strongly confirms its limited self-discharge behavior and superior inhibition on polysulfide shuttling. Apart from that, separators and lithium foils were also extracted after cycling to evaluate the polysulfide shuttling level in batteries based on different sulfur hosts. The optical images clearly show the much brighter and cleaner surfaces of both lithium and separator that coupled with S@PCS electrode (Figure 5d,e). Meanwhile, the energy dispersive X-ray analysis (EDX) spectra also confirms the much lower sulfur content in separator based on S@PCS electrode (Figure 5f), indicating the limited polysulfide dissolution and shutting in the according battery. Furthermore, the scanning electron microscopy (SEM) observation also reveals the considerable smoother lithium surface based on S@PCS electrode (Figure 5g–i), which demonstrates the inhibited anodic corrosion and further corroborates the suppressed polysulfide shuttling in the according configuration.

Raised current densities were further performed to investigate the rate capabilities of S@PCS and S@rGO electrodes. A highly reversible capacity of  $693.3 \text{ mA h g}^{-1}$  was achieved for S@PCS electrode at a high current rate even up to 10 C (Figure 4d). The capacity recovers to  $1059.5 \text{ mA h g}^{-1}$  as the current rate is switched back to C/2. These results manifest the fast reaction kinetics, excellent electrochemical reversibility, and robust electrode integrity for S@PCS electrode. In contrast, S@rGO electrode undergoes a rapid capacity fading along with the increase of the current rate. The superior rate capability of S@PCS electrode is attributed to its favorable electrode construction. The large-area PCS intertwines to build up a conductive framework for fast electron transfer, while the highly porous and polar structure favors electrolyte infiltration for two-phase

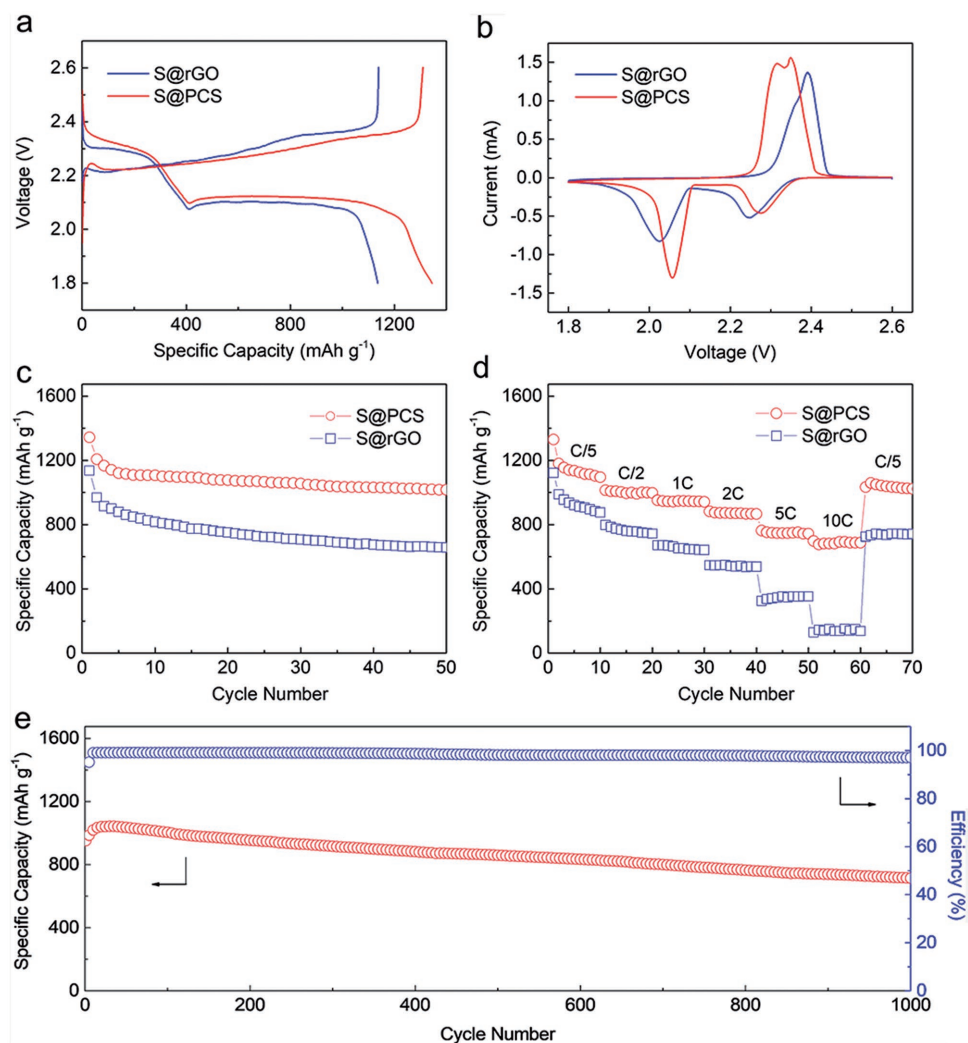


**Figure 4.** The voltage profile a), CV curve b), cycling c), and rate performance d) comparisons between S@PCS and S@rGO electrodes. The long-term cycling performance of S@PCS electrode at 1C over 1000 cycles.

sulfur chemistry. Additionally, the large surface area of PCS also enables a uniform sulfur distribution and abundant electrode/electrolyte interfaces for high-efficiency sulfur electrochemistry. More importantly, the unique porous structure within the carbon sheets establishes an interconnected framework for multidirectional ion transfer, overcoming the lack of vertical ion pathways in conventional graphene-based construction, and thus guarantees a sufficient ion supply and ultrafast sulfur electrochemical redox.

Further electrochemical analyses were performed to verify the benefits of PCS in terms of ion transfer and sulfur electroredox kinetics. **Figure 6a,b** shows the galvanostatic intermittent titration (GITT) profiles of S@rGO and S@PCS electrodes respectively, where the dash lines represent the states of electrochemical equilibration during the multiple rests process. Remarkably, S@PCS electrode exhibits constantly smaller potential gaps between the operating and equilibration states than those for S@rGO electrode, which is clearly revealed by the IR drop variation during the discharge–charge process (**Figure 6c**), demonstrating the much-alleviated polarization

and kinetic limitation in S@PCS electrode. Meanwhile, the constantly higher  $\text{Li}^+$  diffusion coefficients during the discharge–charge revealed by potentiostatic intermittent titration (PITT) analysis evidentially confirms the significantly improved  $\text{Li}^+$  transfer within the S@PCS electrode benefiting from the unique multidirectional ion pathways in PCS matrix (**Figure 6d**). This result also receives strong support from the ex situ EIS study, where the constantly lower Warburg coefficients indicate the easier  $\text{Li}^+$  diffusion in S@PCS electrode (**Figure S9**, Supporting Information). These results mutually confirm the minimized internal resistance and electrochemical polarization benefiting the additional vertical ion pathways offered by the highly porous PCS, which enables the multidirectional ion transfer for fast sulfur electrochemistry (**Figure 6e**). Such unique superiorities endow the S@PCS electrode with much higher energy density and power density than those reported in recent literatures (**Figure S10** and **Table S1**, Supporting Information). Additionally, considering the significance of porosity and element doping, PCSs obtained from precursors with different composition were also prepared to investigate their influence on battery

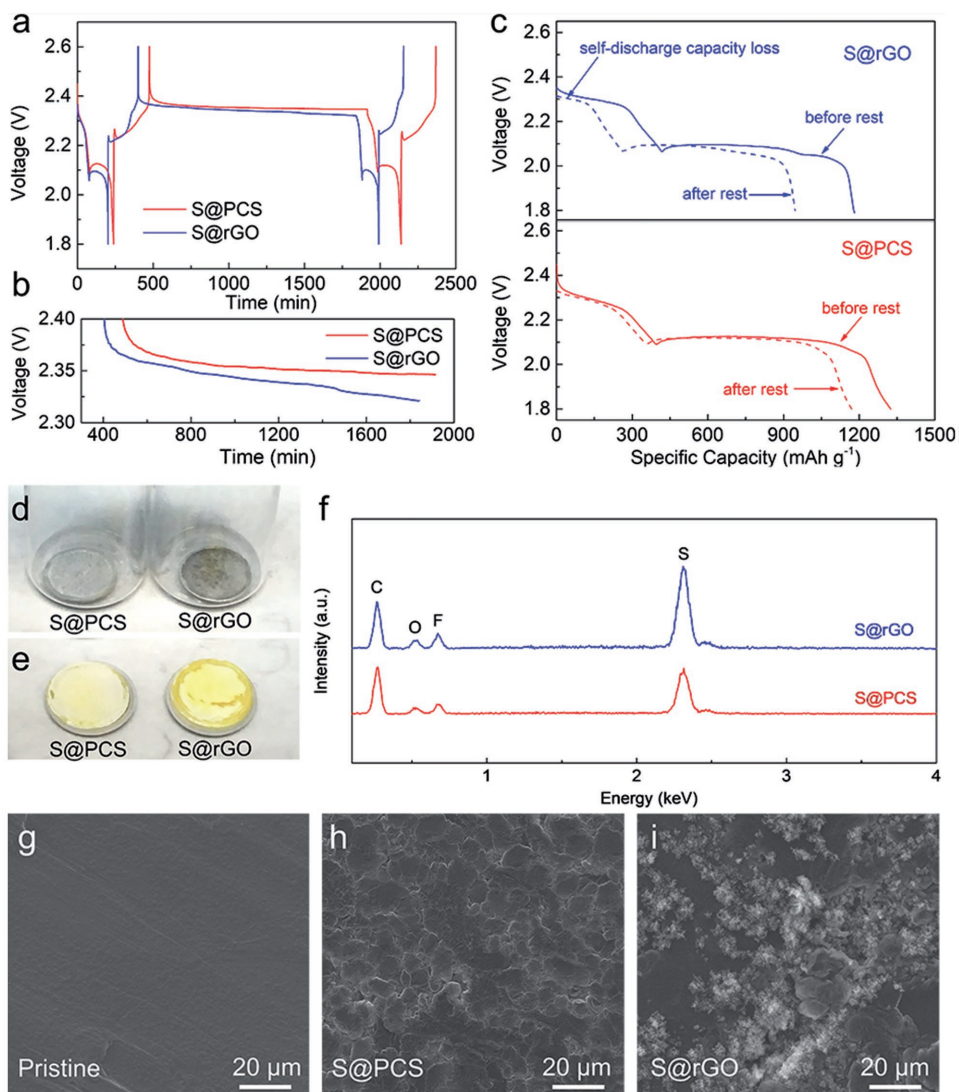


**Figure 5.** The voltage profiles in overall self-discharge test a), the enlarged profiles in the rest process b), and the discharge profiles before and after cell rests c) of S@PCS and S@rGO electrodes; the optical photographs of the lithium anodes d) and separators e), the EDX spectra of the separators f), and the SEM images of pristine lithium anode g), lithium surfaces based on S@PCS h), and S@rGO electrodes i) after 50 cycles.

performance. As shown in Figure S11 (Supporting Information), the porous carbon sheets morphology can be well maintained under different sucrose to  $P_2O_5$  ratios, which signifies the good producibility of this method. The PCS based on the sucrose to  $P_2O_5$  weight ratio of 2:6 exhibits the highest specific surface area and pore volume, as well as the richest element doping, thus yielding the best cycling performance (Figure S12, Supporting Information). In view of the above results, S@PCS electrode was further performed with a long-term operation at 1C rate over 1000 cycles. The electrode reaches its highest capacity of  $1040 \text{ mA h g}^{-1}$  after several cycles activation and achieves an outstanding cyclability with an ultraslow capacity fading rate of 0.025% per cycle, which is much superior than the sulfur electrodes based on 2D carbon materials in recent literatures (Figure 4e and Table S1, Supporting Information).

The practical application of Li-S batteries requires a raised sulfur loading on electrode to output higher energy density.

In this regard, S@PCS electrodes with higher sulfur content (80 and 90 wt%, denoted as S@PCS-80 and S@PCS-90) in composite as well as higher areal sulfur mass loading ( $3.5$  and  $5.5 \text{ mg cm}^{-2}$ ) are attempted for enhanced energy density. The sulfur contents were confirmed by thermogravimetric analysis (TGA) analysis (Figure S13, Supporting Information). As shown in Figure 7a, the favorable porous architecture allows the as-developed PCS to sustain a decent sulfur electrochemistry at a high sulfur content even up to 90 wt%, which is much higher than most in the literatures (Table S1, Supporting Information). However, slightly expanded potential gap can still be observed for electrodes with higher sulfur content due to the lessened conductivity support from the reduced carbon content. It is worth noting that electrodes with high sulfur contents become more competitive in terms of both cyclability and capacity retention when capacity evaluation is performed based on the mass of the composite instead of pure sulfur (Figure 7b,c). In

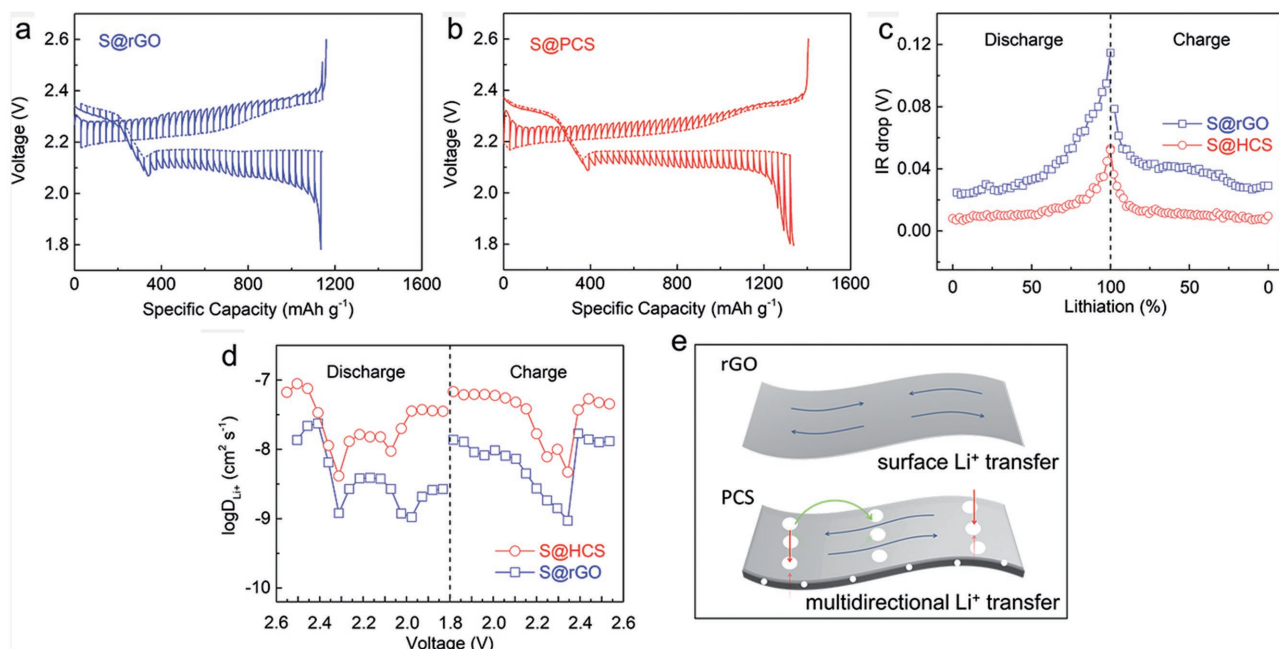


**Figure 6.** The GITT profiles a,b) and the according IR drops during the discharge–charge process of S@rGO and S@PCS electrodes, d) the Li<sup>+</sup> diffusion coefficients of S@rGO and S@PCS electrodes obtained by PITT, e) the simplified schematic of PCS providing additional vertical ion pathway compared to rGO.

such case, S@PCS-80 electrode combines the highest capacity and cyclability, which is thus employed to further promote the areal sulfur loading and energy density. As shown in Figure 7d, S@PCS electrode with a sulfur loading of 5.5 mg cm<sup>-2</sup> yields a high areal capacity of 4.8 mA h cm<sup>-2</sup>, which surpasses that of commercial Li-ion batteries. The stable long-term operation

over 200 cycles also manifests its good cyclability under high sulfur loading (Figure 7e), revealing an intriguing potential of this electrode design for practical use. The great capability of performing sulfur electrochemistry under both high sulfur content and loading relies on the unique porous texture and strong sulfur confinement of PCS. The large-area and highly porous

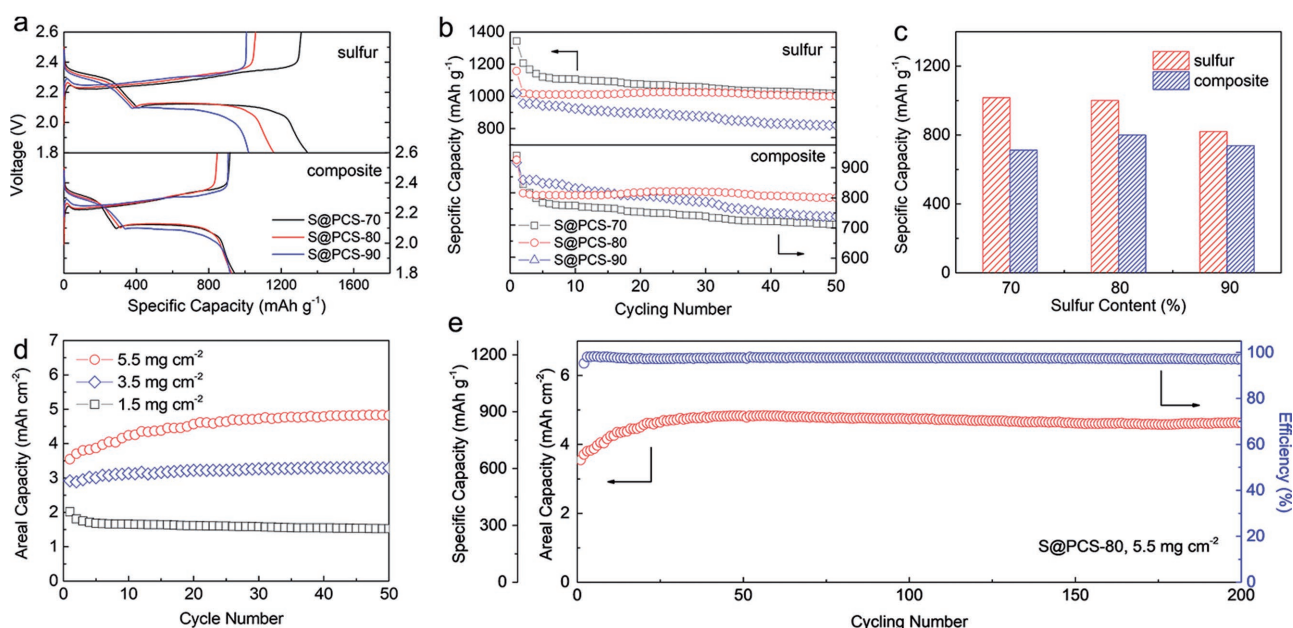


**Figure 7.** The voltage profiles a), cycling performances b), and capacity retentions at 50th cycle c) of S@PCS electrodes with different sulfur contents when capacities were calculated based on sulfur or composite. d) The areal capacities of S@PCS electrode with different sulfur loadings. e) The long-term cycling performance of S@PCS electrode at C/5 rate with sulfur content of 80 wt% and sulfur loading of 5.5 mg cm<sup>-2</sup>.

PCS provides a uniform sulfur distribution, excellent long-term electronic conductivity, and abundant active interfaces for sulfur electrochemistry. Particularly, the polar surface and the massive porous structure of PCS favors a fast and sufficient electrolyte infiltration, and builds up critically the multidirectional pathways for ion transfer, which ensures the sufficient ion supplies and smooth sulfur electroredox under high sulfur loading. Moreover, the synergistically combined physical and chemical confinements of sulfur species further contribute to a high-efficiency inhibition on polysulfide shuttling, thus leading to the reliable sulfur electrochemistry and prolonged battery lifespan.

### 3. Conclusion

In summary, we developed a phosphorous and oxygen dually doped porous carbon sheets through a facile synthesis. The obtained PCS delivers elegant 2D morphology, high porosity, and abundant element doping. When used as sulfur host for Li-S batteries, the large-area intertwined 2D construction offers favorable long-term conductivity, while the inner porosity establishes an admirable 3D architecture framework for multidirectional ion transfer. Meanwhile, a strong sulfur immobilization is realized through the synergistic combination of physical and chemical adsorptions to sulfur species. Attributed to these featuring superiorities, the PCS-based sulfur electrode achieves excellent electrochemical performance, i.e., outstanding cyclability over 1000 cycles, superb rate capability up to 10 C, and high areal capacity of 4.8 mA h cm<sup>-2</sup>. Such an attempt of element-doped porous carbon sheets offers an appealing model of material engineering to promote Li-S performance for practical use, as well as opens up a possibility of favorable structural design in other energy storage and conversion systems including metal ion batteries, supercapacitors, and electrocatalysis.

### 4. Experimental Section

**The Synthesis of PCS and rGO:** The PCS was prepared by using sucrose as carbon source and P<sub>2</sub>O<sub>5</sub> as the single template. Typically, 2.0 g sucrose and 6.0 g P<sub>2</sub>O<sub>5</sub> (in weight ratio of 2:6) were first grinded under low-humidity atmosphere in order to avoid the deliquescence of P<sub>2</sub>O<sub>5</sub>. The mixture was then sealed in a nitrogen-filled 100 mL autoclave and thermally treated at 200 °C for 6 h to gain the precursor, which was subsequently pyrolyzed at 450 °C and 900 °C for 1 and 3 h respectively under Ar atmosphere to yield PCS. The synthesis with different sucrose to P<sub>2</sub>O<sub>5</sub> ratios of 2:1, 2:2, and 2:4 was also performed through the same procedures to study their effects on the morphology and structure of the obtained PCS. Graphene oxide was prepared by modified Hummers' method<sup>[22]</sup> and thermally treated through the same process of PCS to gain the rGO in purpose of comparison.

**Material Characterizations:** SEM (LEO FESEM 1530) and TEM (JEOL 2010F TEM/STEM) were performed for morphology study. The XRD patterns were collected by MiniFlex 600 Rigaku diffractometer. The pore structure was measured by nitrogen sorption (ASAP 2020 micromeritics) and analyzed based on Brunauer–Emmett–Teller theory. The Raman spectrometry was performed with a DXR Raman microscope. The surface chemistry of the samples was analyzed by XPS using Thermo Scientific K-Alpha spectrometer. The electrolyte infiltration observations were performed with a contact angle meter (Cam-plus Micro, Tante

Inc., USA) using the sessile drop technique. UV-vis spectra were collected by Thermo Scientific GENESYS 10S spectrophotometer. TGA was performed by TA instruments Q500 at a heating rate of 5 °C min<sup>-1</sup> under nitrogen atmosphere to confirm the sulfur content.

**Electrochemical Evaluations:** S@PCS was prepared by heating the mixture of elemental sulfur and PCS at 155 °C for 4 h under Ar atmosphere. The sulfur content was controlled by varying the sulfur to PCS weight ratio. The slurry containing S@PCS, super P, and polyvinylidene fluoride in weight ratio of 8:1:1 was casted on Al foil and dried at 60 °C for 12 h to obtain the S@PCS electrode. S@rGO electrode was prepared via the same process in purpose of comparison. The sulfur loading on electrodes for regular tests was around 1.5 mg cm<sup>-2</sup>. Electrodes with higher sulfur loading of 3.5 and 5.5 mg cm<sup>-2</sup> were also fabricated for enhanced energy density. The CR2016 coin cells were assembled using Li foil and Celgard 2325 as counter electrode and separator respectively in Ar-filled glove box with water and oxygen level under 0.5 ppm. The electrolyte contains 1 M LiTFSI with 0.2 M lithium nitrate in binary solvent of DEM and 1,3-dioxolaneDOL (1:1 in volume). The electrolyte addition for each cell was 15 mL g<sup>-1</sup>s. Galvanostatic cycling and multirate tests were performed by LAND battery cycler. The current density and specific capacity were calculated based on the mass of sulfur. GITT tests were performed by alternating pulses (20 min) and open circuit voltage (OCV) periods (2 h). PITT tests were performed with consecutive 0.05 V pulses and 1 h lasting time for each pulse. CV study was recorded by a Gamry 5000E workstation in the voltage range of 1.8–2.6 V (vs Li<sup>+</sup>/Li) at a scan rate of 0.1 mV s<sup>-1</sup>. EIS was also recorded by Gamry 5000E work station in the frequency range of 0.1 Hz–100 kHz.

### Supporting Information

Supporting Information is available from the Wiley Online Library or from the author.

### Acknowledgements

G.R.L. and W.L. contributed equally to this work. This work was supported by the Natural Sciences and Engineering Research Council of Canada (NSERC), the National Natural Science Foundation (21573083), the University of Waterloo, and the Waterloo Institute for Nanotechnology. The authors thank Dr. Navid Bizmark and Dr. Gaopeng Jiang for the contact angle characterizations at University of Waterloo. The authors also thank China Scholarship Council (CSC) for its support.

### Conflict of Interest

The authors declare no conflict of interest.

### Keywords

lithium sulfur batteries, multidirectional ion pathways, porous carbon sheets, reaction kinetics

Received: August 29, 2017

Revised: September 20, 2017

Published online:

[1] a) R. V. Noorden, *Nature* **2013**, 498, 416; b) P. G. Bruce, S. A. Freunberger, L. J. Hardwick, J. M. Tarascon, *Nat. Mater.* **2012**, 11, 19.

[2] a) G. R. Li, M. Ling, Y. F. Ye, Z. P. Li, J. H. Guo, Y. F. Yao, J. F. Zhu, Z. Lin, S. Q. Zhang, *Adv. Energy Mater.* **2015**, 5, 1500878; b) X. Wang, G. Li, J. Li, Y. Zhang, A. Wook, A. Yu, Z. Chen, *Energy Environ. Sci.* **2016**, 9, 2533.

- [3] a) D. Larcher, J. M. Tarascon, *Nat. Chem.* **2015**, *7*, 19; b) A. Manthiram, Y. Fu, S. H. Chung, C. Zu, Y. S. Su, *Chem. Rev.* **2014**, *114*, 11751.
- [4] a) G. R. Li, C. Wang, W. L. Cai, Z. Lin, Z. P. Li, S. Q. Zhang, *NPG Asia Mater.* **2016**, *8*, e317; b) M. Hagen, D. Hanselmann, K. Ahlbrecht, R. Maça, D. Gerber, J. Tübke, *Adv. Energy Mater.* **2015**, *5*, 1401986.
- [5] a) Y. Mao, G. Li, Y. Guo, Z. Li, C. Liang, X. Peng, Z. Lin, *Nat. Commun.* **2017**, *8*, 14628; b) Y. Z. Liu, G. R. Li, J. Fu, Z. W. Chen, X. S. Peng, *Angew. Chem., Int. Ed.* **2017**, *56*, 6176; c) A. Rosenman, E. Markevich, G. Salitra, D. Aurbach, A. Garsuch, F. F. Chesneau, *Adv. Energy Mater.* **2015**, *5*, 1500212.
- [6] A. K. Geim, K. S. Novoselov, *Nat. Mater.* **2007**, *6*, 183.
- [7] a) S. P. Wu, R. Y. Ge, M. J. Lu, R. Xu, Z. Zhang, *Nano Energy* **2015**, *15*, 379; b) C. H. Xu, B. H. Xu, Y. Gu, Z. G. Xiong, J. Sun, X. S. Zhao, *Energy Environ. Sci.* **2013**, *6*, 1388.
- [8] a) H. T. Sun, L. Mei, J. F. Liang, Z. P. Zhao, C. Lee, H. L. Fei, M. N. Ding, J. Lau, M. F. Li, C. Wang, X. Xu, G. L. Hao, B. Papandrea, I. Shakir, B. Dunn, Y. Huang, X. F. Duan, *Science* **2017**, *356*, 599; b) S. Han, D. Q. Wu, S. Li, F. Zhang, X. L. Feng, *Adv. Mater.* **2014**, *26*, 849.
- [9] a) Y. H. Wu, T. Yu, Z. X. Shen, *J. Appl. Phys.* **2010**, *108*, 071301; b) X. Fan, C. Yu, J. Yang, Z. Ling, C. Hu, M. Zhang, J. Qiu, *Adv. Energy Mater.* **2015**, *5*, 1401761; c) Y. Lin, Y. Liao, Z. Chen, J. W. Connell, *Mater. Res. Lett.* **2017**, *5*, 209.
- [10] a) J. H. Liu, X. W. Liu, *Adv. Mater.* **2012**, *24*, 4097; b) H. L. Fan, W. Z. Shen, *Chemosuschem* **2015**, *8*, 2004.
- [11] a) U. K. Sur, *Int. J. Electrochem.* **2012**, *2012*, 237689; b) J. Sánchez-González, A. Macías-García, M. Alexandre-Franco, V. Gómez-Serrano, *Carbon* **2005**, *43*, 741.
- [12] a) A. C. Ferrari, J. C. Meyer, V. Scardaci, C. Casiraghi, M. Lazzeri, F. Mauri, S. Piscanec, D. Jiang, K. S. Novoselov, S. Roth, A. K. Geim, *Phys. Rev. Lett.* **2006**, *97*, 187401; b) A. C. Ferrari, J. Robertson, *Phys. Rev. B* **2000**, *61*, 14095.
- [13] R. Saito, M. Hofmann, G. Dresselhaus, A. Jorio, M. S. Dresselhaus, *Adv. Phys.* **2011**, *60*, 413.
- [14] Z. Z. Sun, Z. Yan, J. Yao, E. Beitler, Y. Zhu, J. M. Tour, *Nature* **2010**, *468*, 549.
- [15] a) R. Li, Z. D. Wei, X. L. Gou, *ACS Catal.* **2015**, *5*, 4133; b) C. Z. Zhang, N. Mahmood, H. Yin, F. Liu, Y. L. Hou, *Adv. Mater.* **2013**, *25*, 4932; c) Y. Y. Wen, B. Wang, C. C. Huang, L. Z. Wang, D. Hulicova-Jurcakova, *Chem. - Eur. J.* **2015**, *21*, 80.
- [16] C. Barchasz, F. Molton, C. Duboc, J. C. Lepretre, S. Patoux, F. Alloin, *Anal. Chem.* **2012**, *84*, 3973.
- [17] Y. S. Su, Y. Fu, T. Cochell, A. Manthiram, *Nat. Commun.* **2013**, *4*, 2985.
- [18] a) T. Z. Hou, W. T. Xu, X. Chen, H. J. Peng, J. Q. Huang, Q. Zhang, *Angew. Chem., Int. Ed. Engl.* **2017**, *56*, 8178; b) Q. Pang, D. Kundu, M. Cuisinier, L. F. Nazar, *Nat. Commun.* **2014**, *5*, 4759.
- [19] a) X. Liang, C. Hart, Q. Pang, A. Garsuch, T. Weiss, L. F. Nazar, *Nat. Commun.* **2015**, *6*, 5682; b) L. Jin, G. Li, B. Liu, Z. Li, J. Zheng, J. P. Zheng, *J. Power Sources* **2017**, *355*, 147.
- [20] N. Tanibata, H. Tsukasaki, M. Deguchi, S. Mori, A. Hayashi, M. Tatsumisago, *J. Mater. Chem. A* **2017**, *5*, 11224.
- [21] X. Li, J. Liang, Y. Lu, Z. Hou, Q. Cheng, Y. Zhu, Y. Qian, *Angew. Chem., Int. Ed.* **2017**, *56*, 2937.
- [22] a) L. Ji, M. Rao, H. Zheng, L. Zhang, Y. Li, W. Duan, J. Guo, E. J. Cairns, Y. Zhang, *J. Am. Chem. Soc.* **2011**, *133*, 18522; b) F. M. Hassan, R. Batmaz, J. Li, X. Wang, X. Xiao, A. Yu, Z. Chen, *Nat. Commun.* **2015**, *6*, 8597.